

# First direct detection of a Keplerian rotating disk around the Be star $\alpha$ Arae using the VLTI/AMBER instrument.

A. Meilland<sup>1</sup>, Ph. Stee<sup>1</sup>, M. Vannier<sup>3</sup>, F. Millour<sup>2</sup>, A. Domiciano de Souza<sup>1,2</sup>, F. Malbet<sup>6</sup>, C. Martayan<sup>4</sup>, F. Paresce<sup>7</sup>, R. Petrov<sup>2</sup>, A. Richichi<sup>5</sup>, and A. Spang<sup>1</sup>

<sup>1</sup> Observatoire de la Côte d'Azur-CNRS-UMR 6203, Département GEMINI, Avenue Copernic, Grasse, France

<sup>2</sup> Laboratoire Universitaire d'Astrophysique de Nice, Parc Valrose, 06108 Nice Cedex 02, France

<sup>3</sup> European Southern Observatory, Cerro Paranal, Chile

<sup>4</sup> GEPI-Observatoire de Paris-Meudon, 5, Place Jules Janssen, 92195 Meudon Cedex, France

<sup>5</sup> European Southern Observatory Karl-Schwarzschild-Strasse 2 D-85748 Garching bei München, Germany

<sup>6</sup> Laboratoire d'Astrophysique de l'Observatoire de Grenoble, 414, Rue de la Piscine, Domaine Universitaire, BP 53, 38041 Grenoble Cedex 09, France

<sup>7</sup> I.N.A.F., Via del Parco Mellini 84, Rome, Italy

Received; accepted

## ABSTRACT

**Aims.** We aim to study the geometry and kinematics of the disk around the Be star  $\alpha$  Arae as a function of wavelength, especially across the Bry emission line. The main purpose of this paper is to answer the question about the nature of the disk rotation around Be stars.

**Methods.** We use the VLTI/AMBER instrument operating in the K band which provides a gain by a factor 5 in spatial resolution compared to previous VLTI/MIDI observations. Moreover, it is possible to combine the high angular resolution provided with the (medium) spectral resolution of AMBER to study the kinematics of the inner part of the disk and to infer its rotation law.

**Results.** We obtain for the first time the direct evidence that the disk is in keplerian rotation, answering a question that occurs since the discovery of the first Be star  $\gamma$  Cas by father Secchi in 1866. We also present the global geometry of the disk showing that it is compatible with a thin disk + polar enhanced winds modeled with the SIMECA code. We found that the disk around  $\alpha$  Arae is compatible with a dense equatorial matter confined in the central region whereas a polar wind is contributing along the rotational axis of the central star. Between these two regions the density must be low enough to reproduce the large visibility modulus (small extension) obtained for two of the four VLTI baselines. Moreover, we obtain that  $\alpha$  Arae is rotating very close to its critical rotation. This scenario is also compatible with the previous MIDI measurements.

**Key words.** Techniques: high angular resolution – Techniques: interferometric – Stars: emission-line, Be – Stars: Keplerian rotation – Stars: individual ( $\alpha$  Arae) – Stars: circumstellar matter

## 1. Introduction

The star  $\alpha$  Arae (HD 158427, HR 6510, B3 Ve), one of the closest ( $d=74$  pc, Hipparcos, Perryman et al. (1997)) Be stars, was observed with the VLTI/MIDI instrument at  $10 \mu\text{m}$  in June 2003 and its circumstellar environment was unresolved even with the 102m baseline (Chesneau et al. (2005), hereafter paper I).  $\alpha$  Arae was a natural choice as first target due to its proximity but also its large mid-IR flux and its high infrared excess among other Be stars, e.g.  $E(V-L)\sim 1.8$  and  $E(V-12\mu\text{m})\sim 2.23$ . These first IR interferometric measurements indicated that the size of the circumstellar environment was smaller than predicted by Stee (2003) for the K band. The fact that  $\alpha$  Arae remain unresolved, but at the same time had

strong Balmer emission, have put very strong constraints on the parameters of its circumstellar disk. Independently of the model, they have obtained an upper limit of the envelope size in the N band of  $\phi_{max}=4$  mas, i.e.  $14 R_{\star}$  if the star is at 74 pc according to Hipparcos parallax or  $20 R_{\star}$  if the star is at 105 pc as suggested by the model presented in paper I.

They finally propose a scenario where the circumstellar environment remains unresolved due to an outer truncation of the disc by an unseen companion. Nevertheless, this companion would be too small and too far away to have any influence on the Be phenomenon itself.

In order to study the inner part of this circumstellar truncated disk we have taken advantage of the higher spatial

resolution by observing at  $2 \mu\text{m}$  with the VLTI/AMBER instrument in February 2005. It provides a gain by a factor 5 in spatial resolution compared to VLTI/MIDI observations. We present in this paper these measurements showing, for the first time, a fully resolved circumstellar envelope in the Bry emission line and a clear signature of a Keplerian rotating disk around  $\alpha$  Arae. We also discuss the challenging question on the nature of the geometry of the Be disks and particularly their opening angle since it is still an active debate.

Following the Wind Compressed Disk model (WCD) by Bjorkman & Cassinelli (1993), most authors have considered geometrically thin disks (half opening angle of 2-5 degrees) even if Owocki et al. (1996) have found that the equatorial wind compression effects are suppressed in any radiatively driven wind models for which the driving forces include a significant part from optically thick lines. Moreover, they found that gravity darkening effects can lead to a reduced mass loss, and thus a lower density in the equatorial regions. A wind compression effect is, however, not required to produce small opening angle of the disk. The investigation of accretion disks has shown that discs in hydrodynamical equilibrium and Keplerian rotation will not have much larger opening angles, since their scale height is governed by the vertical gas pressure only. For a disk to be thicker, either additional mechanisms have to be assumed, or it might not be in equilibrium at the radii in question (Bjorkman & Carciofi 2004).

On the other side, Stee et al. (1995; 1998) claimed that Be disks must be more ellipsoidal in order to reproduce the strong IR excess observed and interpret the possibility for a Be star to change its spectral type from Be to B, and more rarely Be to Be-Shell type, i.e. where the disk is dense enough to produce a strong "shell" absorption.

In the following we adopt, as a starting point, the same parameters for the modeling of  $\alpha$  Arae, e.g. the central star and its circumstellar envelope used in paper I and summarized in Table 1. Following the polarization measurements  $PI \approx 0.6\%$  and Position Angle (PA) of  $172^\circ$  by McLean & Clarke 1979 and Yudin 2001 the disk major-axis orientation is expected to be at about  $PA \approx 82^\circ$  (Wood et al. 1996a, 1996b, Quirrenbach et al. 1997). Assuming a stellar radius of  $4.8 R_\odot$  and an effective temperature  $T_{\text{eff}} = 18\,000 \text{ K}$ , the photospheric angular diameter is estimated to be  $0.7 \text{ mas}$  (Cohen et al. 1998, Chauville et al. 2001). For the distance of  $74 \text{ pc}$  and a baseline of  $60 \text{ m}$  at  $2 \mu\text{m}$ , Stee (2003) predicts the visibility of  $\alpha$  Arae to be lower than  $0.2$ , i.e. fully resolved.

The paper is organized as follows. In Section 2 and 3 we present the interferometric AMBER observations and the data reduction. In Section 4 we try to obtain a first estimate of  $\alpha$  Arae's envelope geometry using very simple "toy" models. Section 5 describes briefly the SIMECA code. In Section 6 we present the best model we obtain with SIMECA that fits both the Bry line and the visibility modulus and phase as a function of wavelength which allows us to infer the disk kinematics and its rotational velocity. Finally, Section 8 draws the conclu-

parameter/result	value
Spectral type	B3Ve
$T_{\text{eff}}$	18 000 K
Mass	$9.6 M_\odot$
Radius	$4.8 R_\odot$
Luminosity	$5.8 \cdot 10^3 L_\odot$
Inclination angle $i$	$45^\circ$
Photospheric density ( $\rho_{\text{phot}}$ )	$1.2 \cdot 10^{-12} \text{ g cm}^{-3}$
Photospheric expansion velocity	$0.07 \text{ km s}^{-1}$
Equatorial rotation velocity	$300 \text{ km s}^{-1}$
Equatorial terminal velocity	$170 \text{ km s}^{-1}$
Polar terminal velocity	$2000 \text{ km s}^{-1}$
Polar mass flux	$1.7 \cdot 10^{-9} M_\odot \text{ year}^{-1} \text{ sr}^{-1}$
m1	0.3
m2	0.45
C1	30
Mass of the disk	$2.3 \cdot 10^{-10} M_\odot$
Mass loss	$6.0 \cdot 10^{-7} M_\odot \text{ year}^{-1}$

**Table 1.** Model parameters for the  $\alpha$  Arae central star and its circumstellar environment obtained from paper I

sions from these first spectrally resolved interferometric measurements of a Be star at  $2 \mu\text{m}$ .

## 2. VLTI/AMBER observations

Our observations of  $\alpha$  Arae were acquired during a Science Demonstration Time (SDT) run, on the nights of 23 and 24 February 2005, using the AMBER instrument on the VLTI in medium-resolution mode ( $R=1500$ ). On the night of 24 February, the observations were made with two UT telescopes, i.e. one interferometric baseline only, and consist of six exposure files, each containing 500 frames of 100 ms. On the following night, three telescopes were used and three-baselines data were taken in a serie of three exposure files and another serie of two, each containing 500 frames of 70 ms. Without a fringe tracker, the integration time per frame must be short enough to minimize the smearing of the fringe visibility due to the beams jitter, while still having enough photons over the elementary exposure. Its specific value is chosen depending on the atmospheric conditions. Immediately after observing  $\alpha$  Arae, a nearby calibrator object was observed.

## 3. Reduction of the interferometric Data

The data has been reduced using the "ammyorick" package developed by the AMBER consortium<sup>1</sup>. The principles of the AMBER data reduction have been described by Millour et al (2005). In addition to the tools furnished by the default package, some specific treatment have been added for reaching an optimal precision on the interferometric observables. The various steps are the following. For each of the individual exposure frames, the complex visibilities are extracted from the various interferometric channels and calibrated using the photometric

<sup>1</sup> see: [http://www-laog.obs.ujf-grenoble.fr/heberges/amber/article.php3?id\\_article=81](http://www-laog.obs.ujf-grenoble.fr/heberges/amber/article.php3?id_article=81)

Date	Timeobs (UTC)	Baselines	Length (m)	P.A. ( $^\circ$ )	Calibrator	$\phi_{\text{cal.}}$ (mas)
24/12/2005	08:46	UT2-4 (B <sub>0</sub> )	80.9	39	HD124454	$1.52 \pm 0.02$
		UT2-3 (B <sub>1</sub> )	46.4	19		
		UT3-4 (B <sub>2</sub> )	52.5	81		
25/12/2005	09:40	UT2-4 (B <sub>3</sub> )	84.6	52	HD124454	$1.52 \pm 0.02$

**Table 2.** Observation log, with the projected baseline lengths and angles. The diameter for the calibrator used is taken from the CHARM catalogue (Richichi & Percheron 2002).

channels and some internal calibration files. The piston  $p$  between the beams is first estimated from the slope of the fringes with wavelength, and a correction phaser is applied on each frame. From this, the color-differential phase and visibility are calculated, for a given spectral channel  $\lambda$ , with respect to a set of reference channel(s). We chose the reference channel to consist in the whole spectral bandwidth except the considered channel  $\lambda$ . Due to the jitter of the beams and to the subsequent variations of output flux after the optical fibers of AMBER, not all the frames contain good quality fringes. A selection and weighing of the best frames above a given threshold is made based on a fringe quality criterion. This yields our color-differential estimators of phase and visibility with an optimal precision. For both the science source and its calibrator, the statistical deviation of the differential phases over the frames serie is about 0.01 rad per spectral channel. The deviation of the normalized differential visibility is about 0.5%. These numbers are similar for all the baselines.

The scaling of the differential visibilities to “absolute” visibilities is done through a best adjustment of the “science” data to the one measured on the calibrator star, whose theoretical visibility is known. For this, the histogram of the squared visibilities from all the science frames (with enough flux above the detector noise) is fitted, by a scaling factor, to the histogram of the calibrator star. With the data we have, this fit has been done globally, by integrating the spectral channels together for each frame. Therefore, some possible bias between the spectral channels would not be suppressed by the calibration process.

In the present case, the observations of the nominal calibrator for  $\alpha$  Arae were of poor quality, and another calibrator, at some distance on the sky ( $\approx 45^\circ$ ), had to be used. This does not seem to affect the calibration, though. The scaling fit between the histograms of the science and calibrator objects results in an error of about 5% on the visibilities, on every baseline.

## 4. Study of the envelope morphology using simple models

In this section we present the new AMBER data with the previous MIDI data already presented in Paper I in order to obtain a first estimate of  $\alpha$  Arae’s envelope geometry using very simple “toy” models.

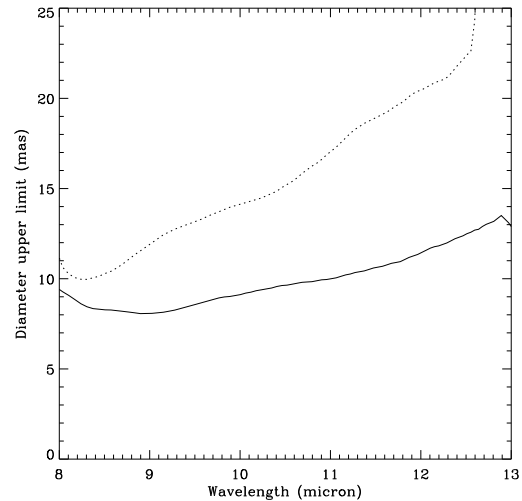


**Fig. 1.**  $\alpha$  Arae (unresolved star + uniform disc) model upper limit diameters (in mas), as a function of wavelength, from the 2005 MIDI data described in paper I for the June, 16 (plain line) and June, 17 nights (dotted line). Note that the large values obtained for larger wavelengths are essentially due to a poor calibration and large error bars rather than a true physical effect.

### 4.1. Envelope extension

#### 4.1.1. Extension in the continuum at $2.1 \mu\text{m}$

Assuming that the visibility we measure in the continuum,  $V_c$ , is only due to the central star and its circumstellar disk we can write:

$$V_c = \frac{V_{ec}F_{ec} + V_{\star c}F_{\star c}}{F_{tot}} \quad (1)$$

where  $V_{ec}$  and  $F_{ec}$  are respectively the envelope visibility and flux in the continuum,  $V_{\star c}$  and  $F_{\star c}$  the star visibility and flux in the continuum and  $F_{tot} = F_{ec} + F_{\star c}$ . Since  $V_c$  is the measured visibility, in order to only estimate the envelope visibility,  $V_{ec}$ , we can rewrite Eq. 1 :

$$V_{ec} = \frac{V_c F_{tot} - V_{\star c} F_{\star c}}{F_{ec}} \quad (2)$$

The total flux is normalized, i.e.  $F_{tot} = F_{ec} + F_{\star c} = 1$ . Since the star is almost unresolved  $0.5 < \phi_{\star} < 0.7$  mas which corresponds to  $0.98 < V_{\star c} < 0.99$  for the longest baseline at  $2.1 \mu\text{m}$ , we assume in the following that  $V_{\star c} = 1$ . In order to estimate  $V_{ec}$  we still have to determine the star and envelope contributions to

the  $2.1 \mu\text{m}$  flux continuum. Since the envelope continuum flux in the visible and in the UV is negligible we have fitted the blue part of the SED using a  $T_{\text{eff}}=18000 \text{ K}$  black body for the central star in order to deduce the envelope emission at larger wavelength. At  $2.1 \mu\text{m}$  we found that the star emission is still  $\sim 1.5$  larger, i.e. 0.44 magnitude brighter, than the envelope contribution thus, following  $F_{\star c}=1.5 F_{ec}$ , we obtain  $F_{\star c}=0.6$  and  $F_{ec}=0.4$ . Equation 2 can now be rewritten as:

$$V_{ec} = 2.5V_c - 1.5 \quad (3)$$

The continuum visibilities and envelope extensions we obtained following Eq. 3, assuming a uniform disk model, are given in table 3.

#### 4.1.2. Extension in the Bry line

We can define the same equation as Eq. 2 for the envelope visibility in the Bry line following:

$$V_{er} = \frac{V_r F_r - V_c F_{tot}}{F_{er}} \quad (4)$$

where  $V_r$  and  $F_r$  are respectively the measured visibility and flux in the Bry line.  $V_c$  and  $F_{tot}$  are the quantities previously defined and  $V_{er}$  and  $F_{er}$  are the visibility and flux only due to the envelope, i.e. without the stellar contribution. We obtain using the Bry emission line profile  $F_{er}=0.5$  and  $F_r=1.5$  at the center of the line. The values of  $V_{er}$  we obtain using Eq. 4 assuming a uniform disk model, are given in Table 3.

Globally, we obtain that, using a simple uniform disk model for each measurement, the Bry emission in the line and the nearby continuum at  $2.1 \mu\text{m}$  have the same extension about 7-8 mas along the UT2-UT3 ( $B_1$ ) and UT3-UT4 ( $B_2$ ) baselines and about 5 mas for UT2-UT4 ( $B_3$ ) and  $\sim 4$  mas for UT2-UT4 ( $B_0$ ) (which was measured at a slightly different PA).

#### 4.2. Comparison between MIDI and AMBER extensions

In order to compare the extensions we obtain with AMBER at  $2.1 \mu\text{m}$  (see Table 3) with the MIDI data presented in paper I, we have calculated the envelope extension in the continuum between 7 and  $13 \mu\text{m}$  following Eq. 2, assuming a uniform disk for each measurement. Unfortunately, these MIDI observations were conducted under unfavorable conditions with thin cirrus passing, and the data were reduced with one of the first versions of the software available. This led to error bars between 8% and 18%, insufficient to measure a significant change of the visibility and thus of the diameter between 7 and  $13 \mu\text{m}$ . Despite these limitations, these measurements have roughly given an upper limit value of the envelope extension around 10 mas in the N band (see Fig. 1) and are compatible with our AMBER measurements.

Moreover, the extension of  $\alpha$  Arae circumstellar environment seems to be almost independent on the wavelength which puts strong constraints on the density law within the envelope. The large upper limit values obtained for larger wavelengths are essentially due to a poor calibration and large error bars

rather than a true physical effect. For "classical" Be stars models, where the density is slowly and regularly decreasing as a function of the distance from the central star, we predict an increasing size as a function of wavelength as shown by Stee (2001). A possibility to keep the same angular size between 2 and  $13 \mu\text{m}$ , may be a disk truncation by an external physical effect as proposed in paper I.

Using FEROS spectroscopic data and the fact that their VLTI/MIDI data are showing a nearly unresolved envelope they propose a possible disk truncation by a unseen companion at a radius of about  $154 R_{\odot}$ , assuming a circular orbit for the companion with negligible mass. With  $R_{\star} = 4.8 R_{\odot}$ , this corresponds to about 32 stellar radii, i.e. 6.4 mas, which is in agreement with their estimate based on the VLTI/MIDI data for a disk truncated at  $25 R_{\star}$ , i.e. 4 mas somewhat smaller than the companion orbit. This is also in agreement with what we have obtained with AMBER, i.e. an envelope extension at  $2.1 \mu\text{m}$  around 7 mas which may appears larger than the 4 mas they obtained. Nevertheless, we must keep in mind that they estimate their extensions using a uniform disk for the star+disk emission whereas we use a unresolved star + a uniform disk only for the circumstellar envelope leading to a larger size.

Finally, we have verified that our best model described in Section 6 was compatible with the MIDI data obtain in 2003 showing a nearly unresolved envelope.

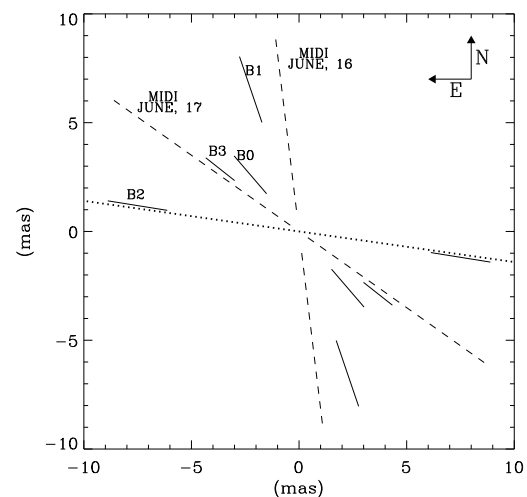


**Fig. 2.**  $\alpha$  Arae (unresolved star + uniform disc) model diameters (in mas) dependence on the baseline position angle. Full line: AMBER measurements in the continuum at  $2.1 \mu\text{m}$ . Dashed lines: MIDI measurements. The length of the plot corresponds to the values of the error bars (note the very large error bars for the MIDI data). The dotted line is the direction of the major-axis of the envelope estimated from polarization measurements (PA= $172^\circ$ ) obtained by McLean & Clarke (1979) and Yudin et al. (1998)

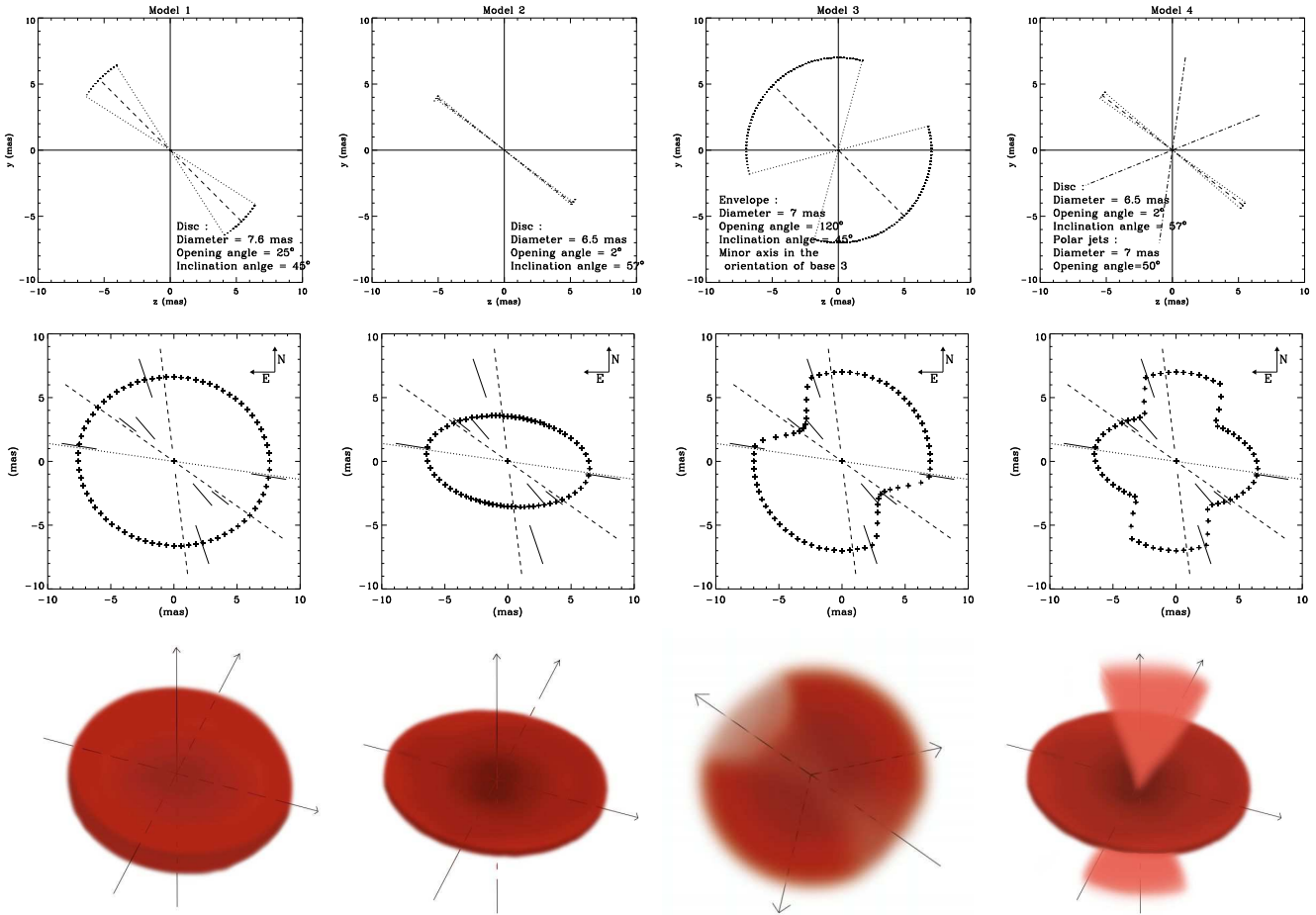


**Fig. 3.** "Toy" models used in order to fit the AMBER and MIDI measurements. The 4 upper pictures are a cut of the circumstellar disk in a plane defined by the observer line of sight and the stellar rotational axis (the observer is on the right for each picture), the corresponding projections into the sky-plane with over-plotted the interferometric data points from MIDI and AMBER are the central pictures whereas a "3D artist view" is plotted into the lower row for each model.

Base n <sup>o</sup>	0	1	2	3
Description	UT2-4	UT2-3	UT3-4	UT2-4
Length (m)	80.9	46.4	52.5	84.6
P.A. (°)	39	19	81	52
$V_c$	0.84	0.80	0.72	0.73
$V_r$	0.63	0.70	0.59	0.55
$V_{ec}$	0.60	0.50	0.30	0.33
$V_{er}$	0.21	0.50	0.33	0.19
$\phi_{ec}$ (mas)	$3.3 \pm 1.2$	$6.8 \pm 1.6$	$7.6 \pm 1.4$	$4.5 \pm 0.9$
$\phi_{er}$ (mas)	$5.3 \pm 2.0$	$6.8 \pm 1.4$	$7.3 \pm 2.1$	$5.2 \pm 1.2$

**Table 3.** Visibilities measured in the continuum at  $2.1 \mu\text{m}$  ( $V_c$ ) and the Bry line ( $V_r$ ) and deduced for the envelope contribution only, using a uniform disk model respectively in the continuum ( $V_{ec}$ ) and in the Bry line ( $V_{er}$ ). The corresponding angular diameters obtained for the envelope are given in the continuum  $\phi_{ec}$  and in the line  $\phi_{er}$ .

### 4.3. Envelope geometry

The envelope extensions presented in Table 3 are very sensitive to the sky-plane baseline orientation. This is particularly obvious from Fig. 2 where we have plotted  $\alpha$  Arae's (unresolved star + uniform disc) model diameters as a function of the sky-plane baseline position. In the following sections we present very simple models in order to constrain the geometry of the circumstellar envelope by fitting the data obtained (see Fig. 2). Note also that we present here models for the light distribution on the sky, not "physical" models which will be presented hereafter.

#### 4.3.1. Equatorial disk perpendicular to the polarization

Our starting point is the equatorial plane position of the circumstellar environment of  $\alpha$  Arae deduced from the polarization measurement done by McLean et Clarke (1979) and Yudin et al. (1998). The polarization angle measured is P.A.= $172^\circ$  and any flattened envelope model should have a semi-major axis perpendicular to this direction, i.e. around  $82^\circ$ .

In the following we consider simple axi-symmetric disk models, presented in Fig. 3, with 3 free parameters:

1. The inclination angle ( $i$ ) between the observer and the polar axis ( $i=0^\circ$  corresponds to pole-on).
2. the opening angle ( $\alpha$ ) of the disk.
3. the disk extension ( $a$ ) in mas.

The shape of the projection of the disk onto the sky-plane depends only on the two first free parameters, i.e.  $i$  and  $\alpha$ . For all these "toy" models the observer is on the right for the 4 upper pictures in Fig. 3. The corresponding projections into the sky-plane with over-plotted the interferometric data points from MIDI and AMBER are the central pictures whereas "3D artist views" are plotted into the lower row for each model.

The ratio between the projected major-axis ( $a$ ) and the minor-axis ( $b$ ) of the envelope is given by:

$$\frac{a}{b} = \frac{1}{\cos i + 2 \sin \frac{\alpha}{4} \sin(i - \frac{\alpha}{4})} \quad (5)$$

We assume that the major-axis of the envelope is oriented at P.A. =  $82^\circ$  (i.e. perpendicular to the polarization angle). Since  $B_2$  is oriented at  $81^\circ$  it is supposed to be a good estimate of the disk major-axis extension. In Fig. 4 we have plotted the ratio  $a/b$  as a function of the disk opening angle for different inclination angles between  $35^\circ$  and  $60^\circ$ . This angle range was determined following the inclination angle of  $45^\circ$  for  $\alpha$  Arae determined from the fit of the circumstellar  $H\alpha$ ,  $H\beta$  and  $P\beta$  emission lines in paper I. From Fig. 4 it is obvious that a precise determination of the inclination angle is mandatory in order to obtain an accurate opening angle estimation.

Our first disk model 1 with  $i=45^\circ$ ,  $\alpha = 25^\circ$  and  $a=7.7$  mas corresponds to a projected ellipse with a  $a/b$  ratio of 1.2. The agreement with the observed data is good excepted for the  $B_3$  and  $B_0$  baselines which present a smaller extension than predicted. In order to fit the data for the  $B_3$  and  $B_0$  baselines we define a model 2 with  $i=57^\circ$ ,  $\alpha = 2^\circ$  and  $a=6.5$  mas, i.e. smaller and very thin compared to model 1. In this latter case the  $a/b$  ratio is 1.85 which allows to fit the  $B_2$  and  $B_3$  baselines and MIDI data but not the  $B_0$  and  $B_1$  baselines. As shown in Fig. 4 model (2), with a very thin disk, is not compatible with an inclination angle of  $45^\circ$  and we were obliged to use a larger inclination of  $57^\circ$ . From Fig. 4 we can see that for an inclination angle of  $45^\circ$  the largest  $a/b$  ratio for a extremely thin disk ( $\alpha \sim 0^\circ$ ) is only 1.41, i.e.  $\sqrt{2}$ . Moreover, changing the inclination angle will change the shape of the  $H\alpha$ ,  $H\beta$  and  $P\beta$  line profiles which were used to infer the value of  $45^\circ$  obtained in paper I. Finally, using a simple disk model with various extensions, opening and inclination angles failed to fit simultaneously the AMBER and MIDI data especially for the  $B_0$  and  $B_3$  baselines which show a smaller extension along the PA =  $39^\circ$  and  $52^\circ$  sky-plane orientation.

#### 4.3.2. Polar-axis along the $B_3$ baseline orientation

Since the extension obtained along the  $B_0$  and  $B_3$  baselines are the smallest ones we may consider that these baselines are close

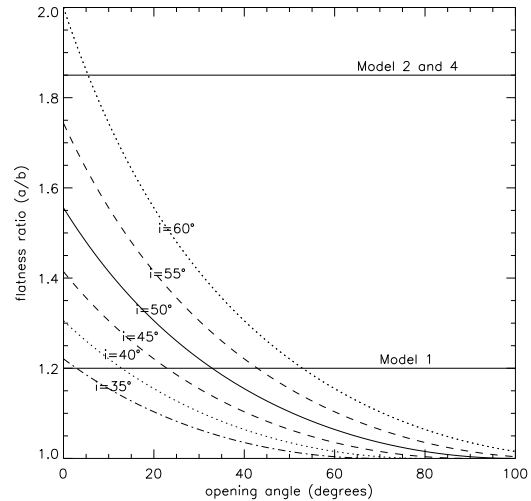


**Fig. 4.** Flatness ratio of the projected envelope versus opening angle calculated with our simple disc model for different inclination angle. Horizontal lines show flatness from model 1 and model 2

to the minor-axis of the envelope (i.e. along the stellar polar-axis). Thus, our model 3 with  $i=45^\circ$ ,  $\alpha = 120^\circ$  and  $a=7.7$  mas is a very thick disk as shown in Fig. 4 with the polar axis close to  $B_0$  and  $B_3$  but thick enough to go through the  $B_1$  and  $B_2$  data points. This model is in fact very similar to the one presented in paper I but in this case it maybe difficult to obtain a polarization large enough to be measured with a PA =  $172^\circ$  since the major-axis of this "disk" is not perpendicular to the polarization direction. Nevertheless, the polarization was measured in the visible, and since it originates from the inner part of the disk, this model cannot be totally excluded.

#### 4.3.3. Equatorial disk + polar enhanced winds

One of the shortcomings of the previous models is that they cannot reproduce simultaneously the two main envelope characteristics : the polarization angle at PA =  $172^\circ$  and the smallest extension along the PA =  $39^\circ$  whereas for the other AMBER baselines the disk is clearly more extended.

Our last simple model 4 try to take into account these observational characteristics by considering an equatorial disk oriented perpendicular to the polarization angle and flattened enough to reproduce the difference between the extension measured along the  $B_0$  and  $B_2$  directions. Moreover, in order to fit the extensions measured for the  $B_1$  baseline, we have added polar enhanced winds perpendicular to the disk as shown in Fig. 3. Thus, seen into the sky plane it is also possible to fit all the interferometric MIDI and AMBER data points. Nevertheless, due to the fact that the disk is geometrically very thin ( $\alpha = 2^\circ$ ) and for the same reasons already explain for our model 2 the inclination angle must be around  $57^\circ$ . Moreover, the polar enhanced winds must be very extended in latitude (with an opening angle about  $50^\circ$ ) and dense enough in order to fit the  $B_1$  measurement.

#### 4.4. Conclusion about the “toy story”

Finally it seems that using very simple “toy” models we failed to reproduce the different extensions of the envelope as a function of the baseline projection onto the sky-plane. Thus, in the following section we will use as a starting point our model 4, i.e. geometrically thin disk + polar enhanced winds which was the one with the better agreement with both AMBER data and polarization direction. Moreover, the formation of geometrically very thin disk, with a few degree for the opening angle seems to be the best scenario up to now, at least for the central Keplerian disk around Be stars.

### 5. The SIMECA code: a brief description

In order to constrain the physical parameters of the circumstellar environment of  $\alpha$  Arae, we have used the SIMECA code. This code, described in previous papers (see Stee & Araújo 1994; Stee et al. 1995; Stee & Bittar 2001), has been developed to model the environment of active hot stars. SIMECA computes line profiles, Spectral Energy Distributions (SEDs) and intensity maps, which can directly be compared to high angular resolution observations. The envelope is supposed to be axi-symmetric with respect to the rotational axis. No meridional circulation is allowed. We also assume that the physics of the polar regions is well represented by a CAK type stellar wind model (Castor et al. 1975) and the solutions for all stellar latitudes are obtained by introducing a parameterized model which is constrained by the spectroscopic and interferometric data. The inner equatorial region is dominated by rotation, therefore being quasi Keplerian. The ionization-excitation equations are solved for an envelope modeled in a  $410 \times 90 \times 71$  cube.

The populations of the atomic levels are strongly altered by non-LTE conditions from their LTE-values. For computation, we start with the LTE populations for each level, and then compute the escape probability of each transition, obtaining up-dated populations. By using these populations as input values for the next step, we iterate until convergence. The basic equations of the SIMECA code are given in detail by Stee et al. (1995).

To take into account the photospheric absorption line, we assume the underlying star to be a normal B3 V star with  $T_{\text{eff}} = 18\,000\text{K}$  and  $R = 4.8R_{\odot}$  and synthesize the photospheric line profiles using the SYNSPEC code by Hubeny (Hubeny 1988; Hubeny & Lanz 1995). The resulting line profile is broadened by solid-body rotation and might be further altered by absorption in the part of the envelope in the line of sight towards the stellar disk.

### 6. Using SIMECA for the modeling of $\alpha$ Arae circumstellar environment

#### 6.1. Fit of the SED

Thanks to the previous study we have now a good starting point for the estimation of the global geometry of the disk around  $\alpha$  Arae. Nevertheless, we want to use the SIMECA model already described in paper I and in section 3 in order to obtain

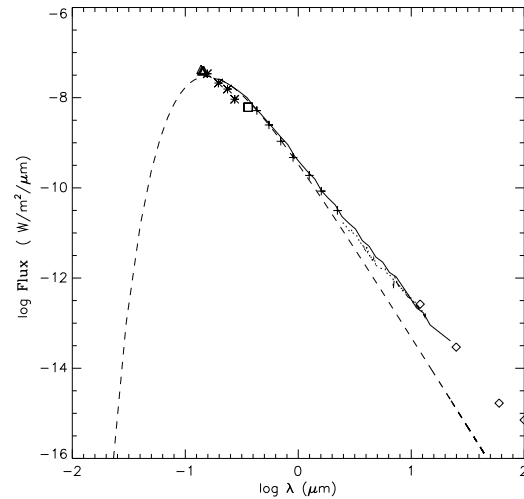


**Fig. 5.**  $\alpha$  Arae’s Spectral Energy Distribution (SED) from various sources in the literature (see text). Dashed line: emission from the central star only assuming a black body with  $R_{\star}=4.8R_{\odot}$ ,  $T_{\text{eff}}=18000\text{K}$  and  $d=105$  pc. Fit of the SED with SIMECA taking into account the envelope free-free and free-bound contribution (plain line) between  $0.3$  and  $20 \mu\text{m}$

a more physical scenario for this star. Thus, in order to obtain a SED which can be used to constrain our model we have collected photometric measurements from the largest spectral range available, i.e. from UV to mid-IR. We used UV measurements from Jamar (1976), Thompson (1978), U magnitude from Johnson (1966), BVRIJHK magnitudes from Ducati (2002), ISO data, MIDI SED measurements (2003) between  $7\text{-}13 \mu\text{m}$  and IRAS data. Of course, using non contemporary data for a variable star may be questionable but this is a good starting point especially for the shorter wavelengths related to the central star which is supposed to be stable, contrary to the circumstellar disk which may appear and vanish with a typical time-scale of a decade and should modify drastically the IR excess of the SED.

The SED we obtain from these various sources is plotted in Fig 5. The SED is dominated by the emission of the central star for wavelengths smaller than  $1 \mu\text{m}$  which is assumed to be a black body with the following parameters from paper I:  $R_{\star}=4.8R_{\odot}$ ,  $T_{\text{eff}}=18000\text{K}$  and  $d=105$  pc. We already discuss in paper I the fact that we were obliged to use a distance of  $105$  pc instead of the  $74$  pc obtained from Hipparcos measurements to fit the SED. Without considering any reddening, and keeping the Hipparcos distance, the radius of  $\alpha$  Arae would be unrealistically low (below  $3.5 R_{\odot}$ ) or the photosphere unrealistically cold ( $T_{\text{eff}} \sim 15000\text{K}$ ) thus we use the  $105$  pc determined from paper I in the following. The free-free and free-bound emissions from the envelope produce an IR-excess and dominate the SED for wavelengths larger than  $\sim 1 \mu\text{m}$  but the envelope remains optically thin. This emission depends mostly on the number of free electrons and on the temperature law in the circumstellar envelope. As the envelope is almost fully ionized, we can consider that the global IR excess is only proportional

to the mass of the disk. In Fig 5 we present our best fit of the SED using a temperature law in the envelope with  $T(r) \propto r^{-3/4}$  and a mass of the envelope of  $4.1 (\pm 0.5) 10^{-10} M_{\odot}$ .

The mass of the disk in SIMECA depends on six parameters: three of them are related to the stellar mass loss: mass flux at the pole,  $C1$ , and  $m1$ . The three other ones are related to the envelope kinematics: terminal velocity at the pole, at the equator and  $m2$ .

The mass flux in SIMECA is given by:

$$\Phi(\theta) = \Phi_{pole}[1 + (C1 - 1) \sin^{m1}(\theta)]. \quad (6)$$

where  $m1$  is the first free parameter which describes the variation of the mass flux from the pole to the equator, and  $C1$  is the ratio between the equatorial and polar mass flux:

$$C1 = \frac{\Phi_{eq}}{\Phi_{pole}}. \quad (7)$$

The expansion velocity field is given by:

$$v_r(r, \theta) = V_o(\theta) + [V_{\infty}(\theta) - V_o(\theta)](1 - \frac{R}{r})^{\gamma}, \quad (8)$$

We used  $\gamma = 0.86$  which is a typical value for early Be stars (Poe & Friend (1986); Araújo & Freitas Pacheco (1989); Owocki et al. (1994)).

with

$$V_o(\theta) = \frac{\Phi(\theta)}{\rho_0} = \frac{\Phi_{pole}[1 + (C1 - 1) \sin^{m1}(\theta)]}{\rho_0}. \quad (9)$$

The second free parameter  $m2$  is introduced in the expression of the terminal velocity as a function of the stellar latitude:

$$V_{\infty}(\theta) = V_{\infty}(pole) + [V_{\infty}(eq) - V_{\infty}(pole)] \sin^{m2}(\theta). \quad (10)$$

**The shape of the terminal velocity law as a function of the stellar latitude is plotted Fig. 7 as well as rotational velocity for various stellar radii.**

Finally the density distribution in the envelope is given by the equation of mass conservation (see Fig. 6):

$$\rho(r, \theta) = \frac{\Phi(\theta)}{(\frac{r}{R})^2 v_r(r, \theta)}. \quad (11)$$

The mass of the disk is obtained by integrating Eq. (11). It is possible to obtain a combination of these six parameters that fit the SED but the solution may of course not be unique. In order to discriminate between all the possible solutions we need to put more constraints on our modeling, namely try to fit the visibility measurements in the lines and in the continuum for the various VLTI baseline orientations.

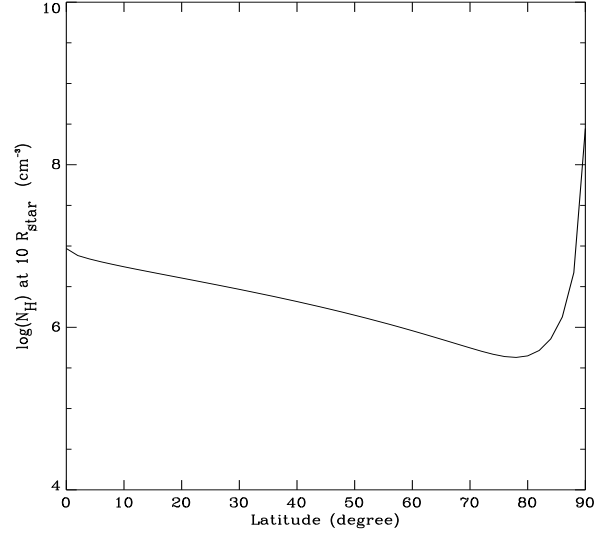


**Fig. 6.** Example of the SIMECA density distribution as a function of the stellar latitude from the pole ( $\theta = 0^\circ$ ) to the equator ( $\theta = 90^\circ$ ) at  $10 R_*$ .

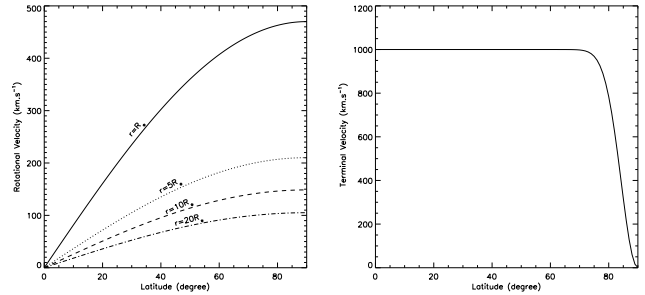


**Fig. 7.** Left: rotational velocities as a function of the stellar latitudes from the pole ( $\theta = 0^\circ$ ) to the equator ( $\theta = 90^\circ$ ) at various stellar radii (over-plotted on the graph). Right: terminal velocity as a function of the stellar latitudes.

## 6.2. Visibility modulus in the continuum

In order to fit the visibility measurements described in section 4.2 we simulate a thin disk + polar enhanced winds with SIMECA with a dense equatorial matter confined in the central region whereas a polar wind is contributing along the rotational axis of the central star. Between these two regions the density must be low enough to reproduce the large visibility modulus (small extension) obtained for the  $B_0$  and  $B_3$  VLTI baselines. Since  $\rho \propto \frac{\Phi}{v_r}$  (see Eq. 11) we can build a model satisfying the above conditions by tuning both the mass flux and the expansion velocity in the envelope. The expansion velocity at the equator should be very small, i.e. a few  $\text{km.s}^{-1}$ , whereas at the pole it can reach larger values up to  $500\text{-}2000 \text{ km.s}^{-1}$ . The density ratio between the equator and the pole must be around 10-100 to fit the data. The parameters we obtain for our best model are given in table 4 and the  $2.15 \mu\text{m}$  intensity map obtained in the continuum is plotted Fig 8. The largest



parameter/result	value
$v \sin i$	$375 \text{ km s}^{-1}$
Inclination angle $i$	$55^\circ$
Photospheric density ( $\rho_{phot}$ )	$1.0 \cdot 10^{-11} \text{ g cm}^{-3}$
Equatorial rotation velocity	$470 \text{ km s}^{-1}$
Equatorial terminal velocity	$1 \text{ km s}^{-1}$
Polar terminal velocity	$1000 \text{ km s}^{-1}$
Polar mass flux	$7 \cdot 10^{-9} M_\odot \text{ year}^{-1} \text{ sr}^{-1}$
m1	0.5
m2	100.0
C1	0.03
Mass of the disk	$4.1 \cdot 10^{-10} M_\odot$
Mass loss	$1.3 \cdot 10^{-8} M_\odot \text{ year}^{-1}$

**Table 4.** Best model parameters for the  $\alpha$  Arae central star and its circumstellar environment obtained from this work. Values for the other parameters that have not changed are listed Table 1 and are from paper I.

discrepancies between these parameters and those from paper I are that the star is now rotating close to its critical velocity ( $v=470 \text{ km s}^{-1}$ , the disk is very thin but denser (by a factor 10)) and the expansion velocity is only  $1 \text{ km s}^{-1}$ . The continuum map is seen with an inclination angle of  $55^\circ$ , the central bright region is the flux contribution from the thin equatorial disk whereas the smoother regions originate from the stellar wind. The brightness contrast between the disk and the wind is  $\sim 30$  but can reach 100 if you compare the inner region of the disk with the outer parts of the wind. This density contrast implies that we use a C1 parameter smaller than 1, i.e. 0.03, in order to keep a sufficient density contrast equator/pole and a negligible equatorial expansion velocity ( $1 \text{ km s}^{-1}$ ).

The fit of the visibility in the continuum basically constrains two parameters : the outer radius of the equatorial disk which will modify the visibilities for all the projected baselines and the inclination angle which have a strong influence on the flattening of the projected equatorial disk into the sky-plane. The outer radius of the equatorial disk for our best model was set to  $33 R_\star$  which is larger compared to the  $25 R_\star$  found in Paper I but still in agreement with the  $32 R_\star$  obtained for the companion orbit. Moreover, the inclination angle we obtain with our best model is  $55 \pm 5^\circ$  which is also larger but in agreement with the inclination angle of  $45 \pm 5^\circ$  found in paper I.

### 6.3. Line profiles

In order to put additional constraints on our modeling we also try to fit emission line profiles with SIMECA, namely  $H\alpha$ ,  $H\beta$  and  $Pa\beta$ . These lines were also used in paper I but following a quite different scenario: a nearly spherical expanding and rotating envelope versus a thin disk + polar wind in this paper. Moreover, we also used in this paper the  $Bry$  emission line which is accessible to AMBER. We remind that the  $H\alpha$  and  $H\beta$  line profiles were observed in April 1999 with the HEROS instrument at la Silla (Chile), the  $Pa\beta$  profile was recorded in August 13, 2003 at the Observatorio do Pico dos Dias (Brasil)

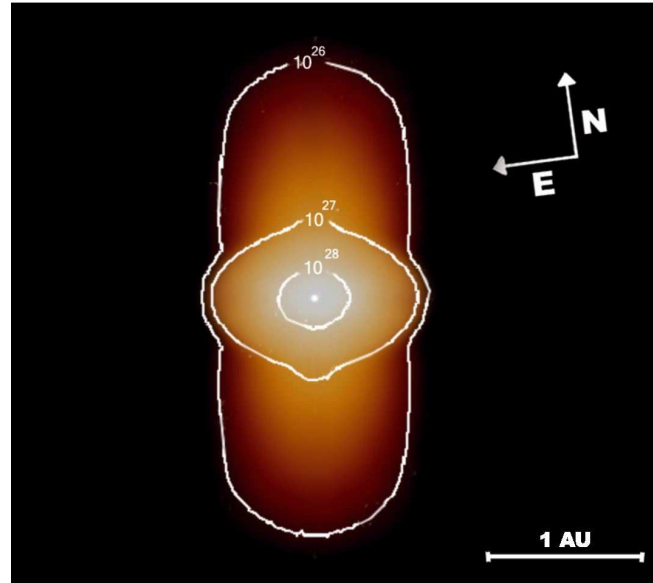


**Fig. 8.** Intensity map in the continuum at  $2.15 \mu\text{m}$  obtained with SIMECA for our best model parameters. The inclination angle is  $55^\circ$ , the central bright region is the flux contribution from the thin equatorial disk whereas the smoother regions originate from the stellar wind. The brightness contrast between the disk and the wind is globally  $\sim 30$  but can reach 100 if you compare the inner region of the disk with the outer parts of the wind.

and only the  $Bry$  line was contemporary to our AMBER interferometric observations. Knowing that  $\alpha$  Arae is a variable star exhibiting line variations with typical time scales of a few months, we will only use the global shape of these line profiles in order to constrain the kinematics within the disk. We will not try to fit simultaneously the intensity of all these lines which is, moreover, not possible as shown in paper I. In our new model these emission lines originate from the dense and thin equatorial disk and thus a fit of the shape of these lines will put strong constraints on the disk kinematics which is supposed to only rotate around the central star. Again, this is a quite different scenario compared to paper I where we used an expanding and rotating nearly spherical envelope to fit the lines.

The observed  $Bry$  line profile is not showing a double-peaks structure due to the medium (1500) AMBER spectral resolution mode used for these first interferometric observation since the high (10000) AMBER spectral resolution mode was not available at this time. Nevertheless, we can see in Fig.9 that after a convolution with a  $15 \text{ \AA}$  gaussian, corresponding to the AMBER spectral resolution, the agreement with the modeled profile (lower row, right profile, dashed line) and the AMBER ones (plain line) is satisfying. For the other lines the fit of the peaks separation is in agreement with the keplerian rotation. As already discussed in paper I, we recall that between the 1999 observations ( $H\alpha$  and  $H\beta$  profiles), the 2003 ( $Pa\beta$ ) and 2005 ( $Bry$ ) observations, we have decreased the density at the base of the stellar photosphere by 25 % in order to fit the line intensity.

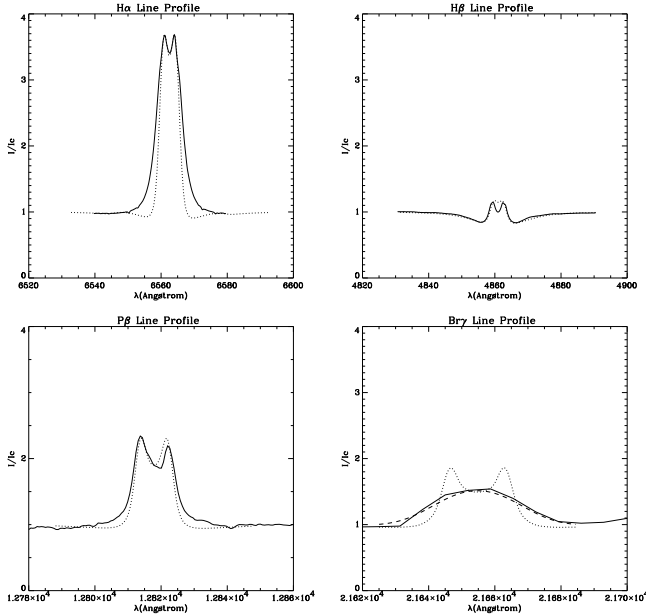


**Fig. 9.** Line profiles modeled with the SIMECA code using a thin disk + polar wind scenario. Modeled profiles are dotted lines whereas observed ones are in plain line. For  $\text{Br}\gamma$  we have convoluted the modeled profile (dotted line) obtain with SIMECA with a  $15 \text{ \AA}$  gaussian, corresponding to the AMBER spectral resolution of 1500. The convoluted  $\text{Br}\gamma$  profile we obtain is the dashed line superimposed with the observed one (plain line).

Compared to paper I, the agreement between the modeled (dotted line) and observed (plain line)  $\text{H}\alpha$  line profile in Fig. 9 is not as good. We are not able to reproduce the broad line wings which were mainly due to the nearly spherical expanding stellar wind used in our previous model. In our new scenario the geometrically thin and rotating equatorial disk produces a narrower  $\text{H}\alpha$  line profile. In order to obtain larger line widths we should have taken into account multiple diffusion that occurs preferentially in the line wings as shown by Poekert & Marlborough (1979). This is especially true for  $\text{H}\alpha$  and  $\text{Pa}\beta$  but less pronounced for  $\text{H}\beta$  and  $\text{Br}\gamma$ . Nevertheless, we concentrate ourselves to the double-peaks separation which is very sensitive to the rotational velocity law used and as already mentioned, the agreement we obtain was better using a keplerian rotating law within the disk.

#### 6.4. Differential visibility modulus across the $\text{Br}\gamma$ emission line

The differential visibilities curves are plotted Fig. 10 for the  $\text{B}_0$ ,  $\text{B}_1$ ,  $\text{B}_2$  and  $\text{B}_3$  baselines. The agreement between the modeled visibility (plain-lines) and the VLTI/AMBER data is very good. Moreover, it was possible to reproduce the visibility decrease across the  $\text{Br}\gamma$  line profile mainly due to the variation of the flux ratio between the unresolved star and the partially resolved circumstellar environment but also its shapes as a function of wavelength. For the  $\text{B}_2$  baseline mainly along the equatorial

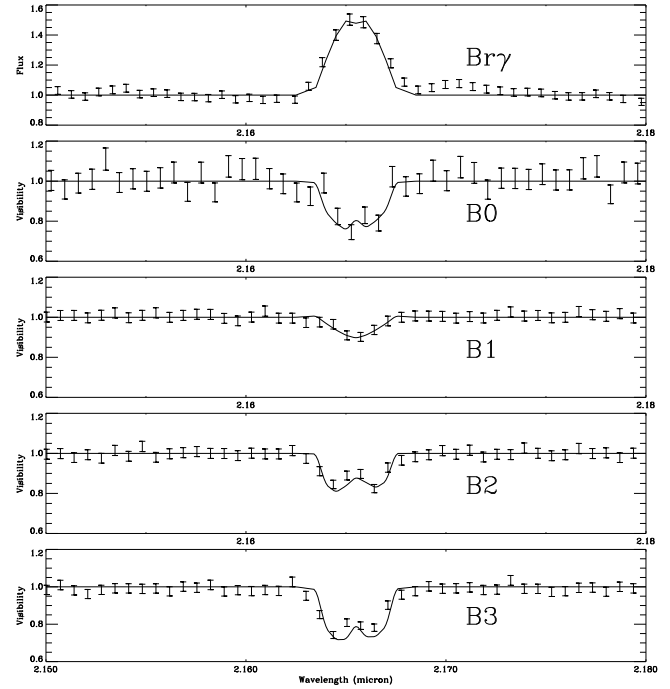


**Fig. 10.** Differential visibility across the  $\text{Br}\gamma$  line profile for the  $\text{B}_0$ ,  $\text{B}_1$ ,  $\text{B}_2$  and  $\text{B}_3$  baselines. The first picture from the top is the  $\text{Br}\gamma$  line profile. The plain line are the fits we obtain with SIMECA from our best model whereas the VLTI/AMBER data are the points with error bars.

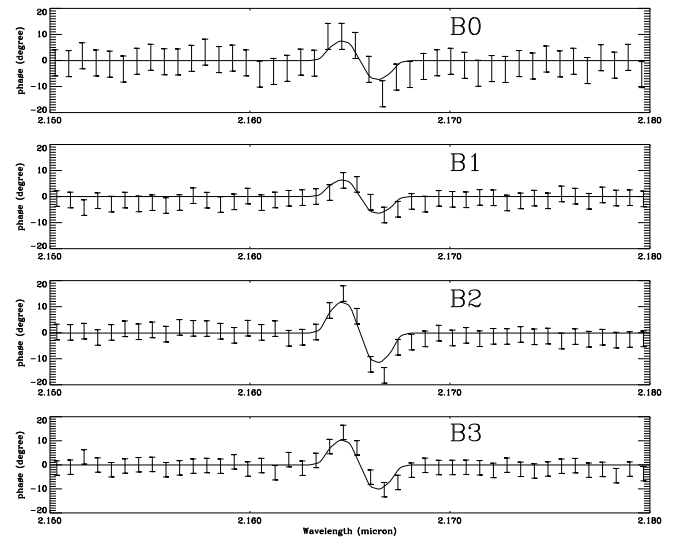


**Fig. 11.** Phase of the visibility across the  $\text{Br}\gamma$  line profile for the  $\text{B}_0$ ,  $\text{B}_1$ ,  $\text{B}_2$  and  $\text{B}_3$  baselines. The plain line are the fits we obtain with SIMECA from our best model whereas the VLTI/AMBER data are the points with error bars.

disk direction, the  $\text{B}_0$  and  $\text{B}_3$  baselines close to the equatorial disk, the curves, with a global "U" shape, present a visibility increase at the center of the line. This means that  $\alpha$  Arae observed within a narrow spectral bandwidth of  $15 \text{ \AA}$  appears smaller at the center of the emission line compared to its extension in the

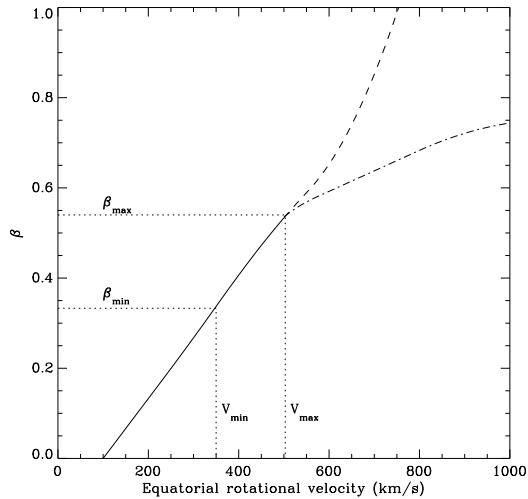


**Fig. 13.**  $\beta$  parameter as a function of the equatorial velocity taking into account the stellar photosphere deformation due to its fast rotation. The plain line corresponds to physically possible cases whereas the dashed line corresponds to rotational values larger than the "breakup" velocity. The dash-dotted line also corresponds to unrealistic values but in this case we have not taken into account the stellar photosphere distortion larger than  $1.5 R_{\star}$  at the equator.  $v_{min}=351 \text{ km s}^{-1}$  corresponds to the minimum  $v \sin i$  found in the literature for this star, i.e.  $288 \text{ km s}^{-1}$ , by Uesugi & Fukuda (1970) with  $i=55^{\circ}$ .

nearby emission line wings as seen in Fig.12. On the contrary, for the  $B_1$  baseline oriented along the polar-axis the visibility curve present a single "V" shape decrease at the line center. These effects are mainly due to the kinematics within the disk and are confirmed by the shape of the phase of the visibility as we will see in the following section.

### 6.5. Differential phase across the $B_{\gamma}$ emission line

The shape of the differential phase across the  $B_{\gamma}$  line profile is related to the photocenter displacement of the object as a function of wavelength and is very sensitive to the  $\beta$  law used in the modeling as already shown by Stee (1996). For our best model we used a keplerian rotation within the disk and the resulting visibility phases as a function of wavelength for the  $B_0$ ,  $B_1$ ,  $B_2$  and  $B_3$  baselines are plotted Fig. 11. Again, the agreement between the modeled phases and the VLTI/AMBER data is very good which is the **first direct evidence of the keplerian rotation within a Be circumstellar disk**. Nevertheless, in order to know if this agreement is unique we have tested different models with different disk rotational velocities following:

$$v_{\phi}(r, \theta) \propto \sin \theta \left( \frac{R}{r} \right)^{\beta}, \quad (12)$$

with  $\beta$  between the constant rotation ( $\beta = 0$ ) and the angular momentum conservation ( $\beta = 1.0$ ), respectively  $\beta=0, 0.3, 0.4, 0.45, 0.5, 0.55, 0.7$  and  $1$ . Nevertheless, if you modify

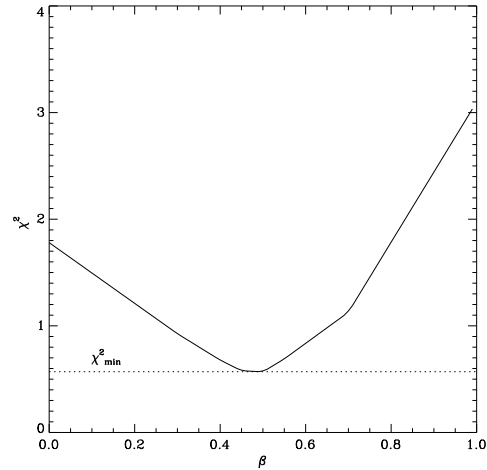


**Fig. 14.**  $\chi^2$  from our models and the AMBER data plotted as a function of the  $\beta$  parameter.  $\chi^2_{min}$  is the minimum value obtained for a model with  $\beta=0.48$  which is very close to the Keplerian rotation ( $\beta=0.5$ ).

the  $\beta$  law and still want to fit the double-peaks of the  $B_{\gamma}$  emission line profile you need to simultaneously modify the equatorial rotational velocity of the star since the inner part of the disk, supposed to be in contact with the star's photosphere, rotates at the same velocity. Thus we were obliged to take into account the shape of the star photosphere and its distortion due to its fast rotational velocity as shown by Domiciano de Souza et al.(2003) for the Be star Achernar which was rotating close to its critical velocity and thus exhibit a flattened photosphere with an equatorial vs polar radius ratio of 1.5. In Fig. 13 we have plotted the "beta" law versus the equatorial rotational velocity that fit the double-peaks of the  $B_{\gamma}$  line emission line profile, assuming a purely circumstellar rotating disk without expansion. This figure shows that if we assume that the stellar rotation is between  $v_{min}$  corresponding to the smaller measured  $v \sin i = 288 \text{ km s}^{-1}$  by Uesugi & Fukuda (1970), with  $i=55^{\circ}$ , i.e.  $v_{min} = 350 \text{ km s}^{-1}$  and  $v_{max}$ , corresponding to the critical velocity for this star, i.e.  $v_{max} = 503 \text{ km s}^{-1}$ ; the  $\beta$  parameter must lie between 0.33 and 0.54. This last value is in better agreement with the upper value of the measured  $v \sin i = 375 \text{ km s}^{-1}$  by Bernacca & Perinotto (1970) with  $i=55^{\circ}$ , i.e.  $v = 457 \text{ km s}^{-1}$  at the equator which may be a good indication that  **$\alpha$  Arae is rotating very close to its critical velocity.**

Moreover, in order to be more quantitative we have computed the total  $\chi^2$  from our best model as a function of the  $\beta$  parameter. The results are plotted Fig.14 and we clearly see that the better agreement ( $\chi^2_{min}$ ) is obtained for a rotating law very close to the Keplerian rotation, i.e.  $\chi^2_{min} = 0.48 \pm 0.04$ .

### 6.6. Is the geometrically thin and rotating disk scenario unique ?

Since our Keplerian disk + polar enhanced winds scenario seems to successfully reproduce all the available observables

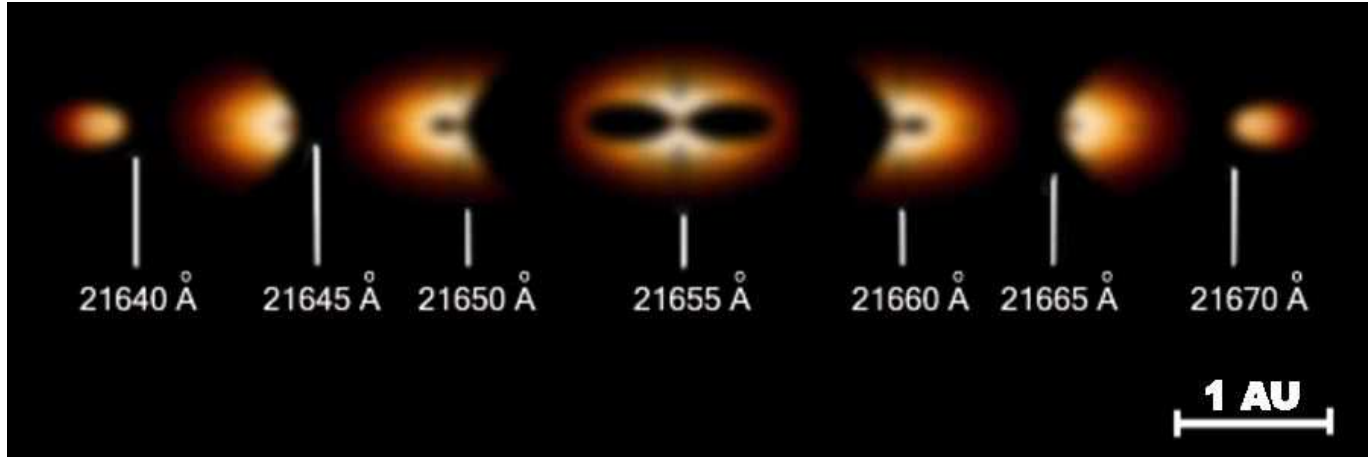


**Fig. 12.** Intensity maps across the Br $\gamma$  line profiles within spectral channels of 15 Å from which the differential visibility modulus and phase are estimated. Note that in order to increase the image contrast the central star and the continuum emission has been subtracted.

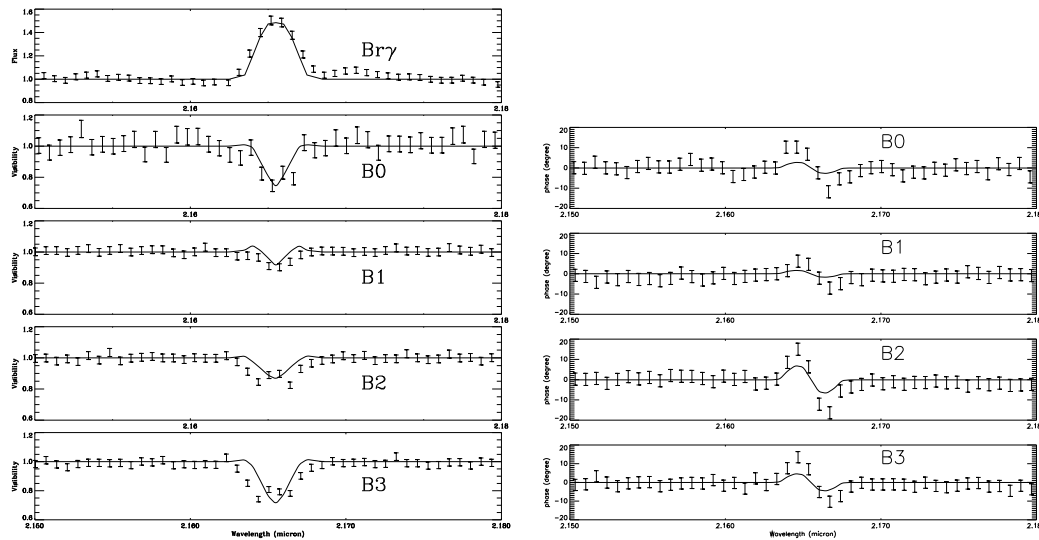


**Fig. 15.**  $\alpha$  Arae differential visibilities (left) and phases (right) across the Br $\gamma$  line profiles for the B<sub>0</sub>, B<sub>1</sub>, B<sub>2</sub> and B<sub>3</sub> baselines. The plain line are the fits we obtain with SIMECA from a rotating and expanding scenario described in section 6.6 whereas the VTI/AMBER data are the points with error bars

(i.e. photometric, spectroscopic, polarimetric and interferometric) we may wonder if this scenario is really unique, especially due to the number of parameters used in the SIMECA code. Thus, we have tested two other scenarios, the first one is based on the same global geometry of our best model, but we have now added an expansion component produced by an equatorial stellar wind.

Since the peaks separation of the line profiles depends on both components of the velocity field, i.e. expansion and rotation, we have to decrease the rotational velocity used in our best model to keep the same observed peaks separation. Remembering that the lowest possible value of the rotational velocity is  $35 \text{ km s}^{-1}$  we can only use a maximum value of  $100 \text{ km s}^{-1}$  for the expansion equatorial terminal velocity. The

corresponding differential visibilities and phases we obtain are plotted Fig. 6.5. In this case, the decrease of the differential phase amplitude variations is due to the smaller value used for the rotating component. If the envelope was only in spherical expansion due to a spherical stellar wind, the phase variation across the Br $\gamma$  line would be zero since there is no photocenter displacement for a spherically symmetric velocity field. On the contrary, if you have a purely rotating disk, the photocenter displacement will follow the projection of the iso-velocities regions and will produce a typical “S-shape” as shown Fig. 11. Thus, a decrease of the rotational velocity field component regarding the expansion component produces globally a smaller differential phase amplitude variation shown Fig. 14. The amplitude of the differential visibility across the line remains almost the same since it is less sensitive to the

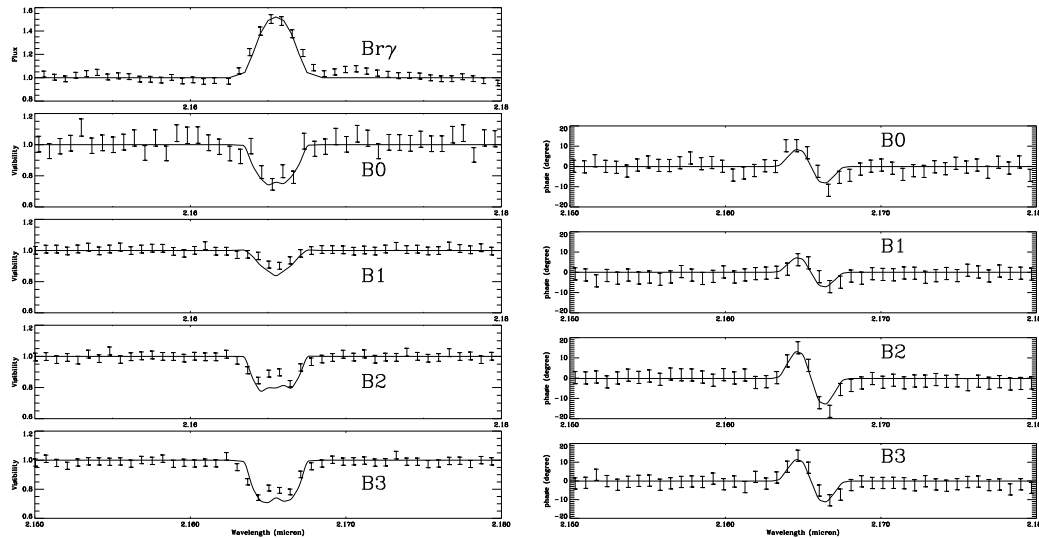


**Fig. 16.**  $\alpha$  Arae differential visibilities (left) and phases (right) across the Br $\gamma$  line profiles for the B<sub>0</sub>, B<sub>1</sub>, B<sub>2</sub> and B<sub>3</sub> baselines. The plain line are the fits we obtain with SIMECA from the model 3 described in section 4.3.2 and section 6.6 whereas the VLT/AMBER data are the points with error bars

kinematics within the disk but rather to a global geometric change of the circumstellar environment and to a change in the star versus envelope flux ratio in the line and the continuum which remains unchanged by modifying the velocity fields. Nevertheless, the shape of the differential visibility is strongly modified and presents now a “V” shape as already mentioned in section 6.4. This shape variation is due to the fact that the expansion versus rotation ratio is increasing in the equatorial region and the difference between the pole versus equator kinematics is less pronounced when adding an equatorial expansion component. This analysis exhibit the importance of spectrally resolved interferometric measurements for the study of the kinematics within circumstellar disks.

The second scenario is based on a quasi-spherical model as the model 3 already described in our “toy story” section. The kinematic used is very close to our thin disk + polar enhanced winds model, (i.e. Keplerian rotation with a  $1\text{km}^{-1}$  equatorial terminal velocity) but in this later case the disk is rather geometrically thick. Again, the corresponding differential visibilities and phases we obtain are plotted Fig. 15. Since the kinematics remains mostly unchanged the fits of the differential phases are as good as for our best model but since the geometry of the disk is different the agreement with the differential visibilities is not as good. Again, thanks to the same disk kinematics the shape of the differential visibilities is very similar but their amplitudes are not well reproduced. Nevertheless, these differences remain very small for an inclination angle of  $55^\circ$  and it is very hard to put an upper limit for the disk opening angle using this method, especially regarding the actual errors on the AMBER absolute calibrated visibilities. On the other side this study clearly shows that the equatorial region is a Keplerian rotating disk rather than an expanding wind.

## 7. Discussion

This study point out three important results touching lively debated issues:

### 7.1. Keplerian rotation

There were already some indications that the disk may follow the Keplerian rotation by other theoretical studies, for instance the results obtained by Hanuschik (1995) regarding shell lines produced within a Keplerian disk in hydrostatic equilibrium. Hanuschik (1996); (2000) also investigate the geometrical structure of the emitting part of circumstellar envelopes around Be stars and found a good agreement with spectroscopic data using a thin disk in vertical hydrostatic and horizontal centrifugal equilibrium, similar to a Keplerian accretion disk. These results were confirmed by Rivinius (1999) presenting high resolution echelle spectra for 6 B-type stars supposed to be seen edge-on and in good agreement with Hanuschik’s models for the formation of shell lines in circumstellar disks with Keplerian rotation. In a more recent paper Rivinius (1999) propose a scenario where the disk is no more a completely stationary structure but rather a succession of outbursts which may form rings. But even within this scenario, part of the ejected matters attains sufficiently high angular momentum to form a roughly Keplerian disk, at least for the immediate times of outbursts. Finally, another indirect argument in favor of a Keplerian disk is the success of the global oscillation modeling already outlined in the paper review by Porter & Rivinius (2003). Thus, our results may be the way to put a final exclamation mark regarding the widely accepted fact that **circumstellar disk around Be stars are in Keplerian rotation.**

## 7.2. Stellar rotation

As already mentioned in section 6.5 we found that  $\alpha$  Arae must be **rotating very close to its critical velocity** since we obtain  $\frac{v_{rot}}{v_{crit}} \sim 91\%$ . This value is far above the conservative estimates of  $\sim 75\%$  usually found in the literature for Be stars. The fact that Be stars may be rotating much closer to their critical velocities than it is generally supposed was already outlined by Townsend et al. (2004) and Owocki (1996). This nearly critical rotation has quite profound implications for dynamical models of Be disk formation and may be the clue for the Be phenomenon. It may bring sufficient energy to levitate material in a strong gravitational field or at least help other physical processes such as pulsation or gas pressure to provide sufficient energy and angular momentum to create a circumstellar disk. Moreover, observational evidences of this nearly critical rotation are growing such as the results obtained by Domiciano et al. (2003) using interferometric VLTI/VINCI data of Achernar. They measured a rotationally distorted photosphere with an apparent oblateness of 1.56 which cannot be explained using the classical Roche approximation. This scenario follows the original picture by Struve (1931) of a critically rotating star, ejecting material from its equatorial regions.

## 7.3. Polar wind enhancement

Our interferometric measurements are evidencing a **polar wind enhancement** (see Fig. 8) which was already predicted for almost critically rotating stars. For instance, Cranmer & Owocki (1995) and Owocki & Gayley (1998) studied the effects of limb darkening, gravity darkening and oblateness on the radiation driving mechanism and found that the tendency for the higher flux from the bright poles to drive material toward the darker equatorial region is outweighed by the opposite tendency for the oblateness of the stellar surface to direct the radiative flux to higher latitudes, i.e. away from the equator. The paper review by Porter & Rivinius (2003) also outline the effect of the inclusion of nonradial line-driving force which reduces the effect of the wind compression to zero and, taking into account the gravity darkening, results in a polar wind enhancement. This physical effect goes in the opposite direction to the one proposed for the Wind Compressed Disk model from Bjorkman & Cassinelli (1993). In a recent paper, Kervella & Domiciano de Souza (2006) have evidenced an enhanced polar wind for the Be star Achernar whereas this Be star presents no hydrogen lines in strong emission. Thus, it seems that a significant polar wind may be present even if the star is still in a normal B phase, i.e. this enhanced polar wind does not seem to be related to the existence of a dense equatorial envelope, as already outlined by Kervella & Domiciano de Souza (2006).

## 8. Conclusion

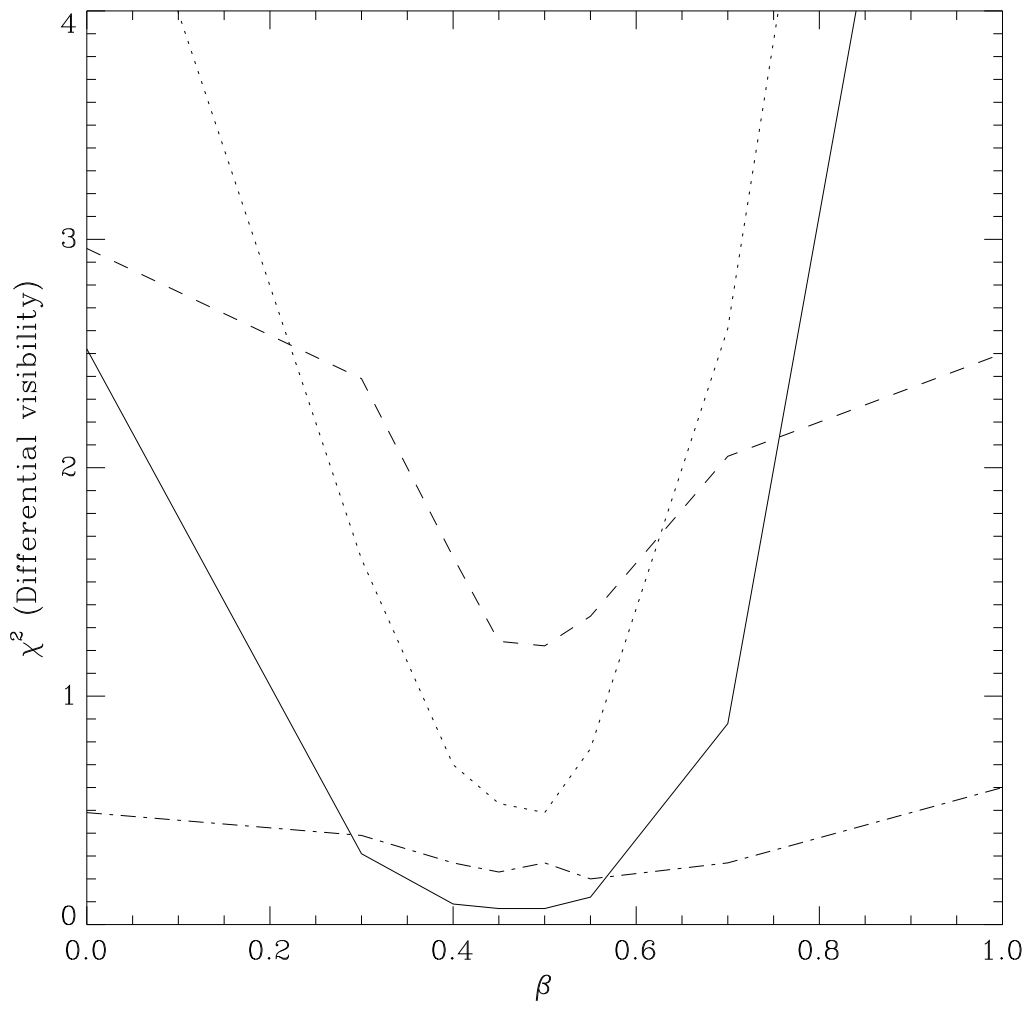
1. Thanks to these first spectrally resolved interferometric measurements of a Be star at  $2 \mu\text{m}$  we are able to propose a possible scenario for the Be star  $\alpha$  Arae's circumstellar environment which consist in a thin disk + polar enhanced winds that is successfully modeled with the SIMECA code.
2. We found that the disk around  $\alpha$  Arae is compatible with a dense equatorial matter confined in the central region whereas a polar wind is contributing along the rotational axis of the central star. Between these two regions the density must be low enough to reproduce the large visibility modulus (small extension) obtained for two of the four VLTI baselines. This new scenario is also compatible with the previous MIDI measurements and the fact that the outer part of the disk may be truncated by a unseen companion at  $32 R_{\star}$ .
3. We obtain for the first time the clear evidence that the disk is in Keplerian rotation, closing a debate that occurs since the discovery of the first Be star  $\gamma$  Cas by father Secchi in 1866.
4. We found that that  $\alpha$  Arae must be rotating very close to its critical velocity.
5. These observations were done using the medium (1500) spectral resolution of the VLTI/AMBER instrument and are very promising for the forthcoming AMBER high spectral resolution observational mode (10000) and the coupling of the Auxiliary Telescopes (ATs) on the VLTI array.

*Acknowledgements.* This research has made use of SIMBAD database, operated at CDS, Strasbourg, France. We thanks G. Duvert and J.M. Clausse for their help in the data reduction through the JMMC. We acknowledge the useful comments of the referee Thomas Rivinius who really help to improve the discussion in this paper.

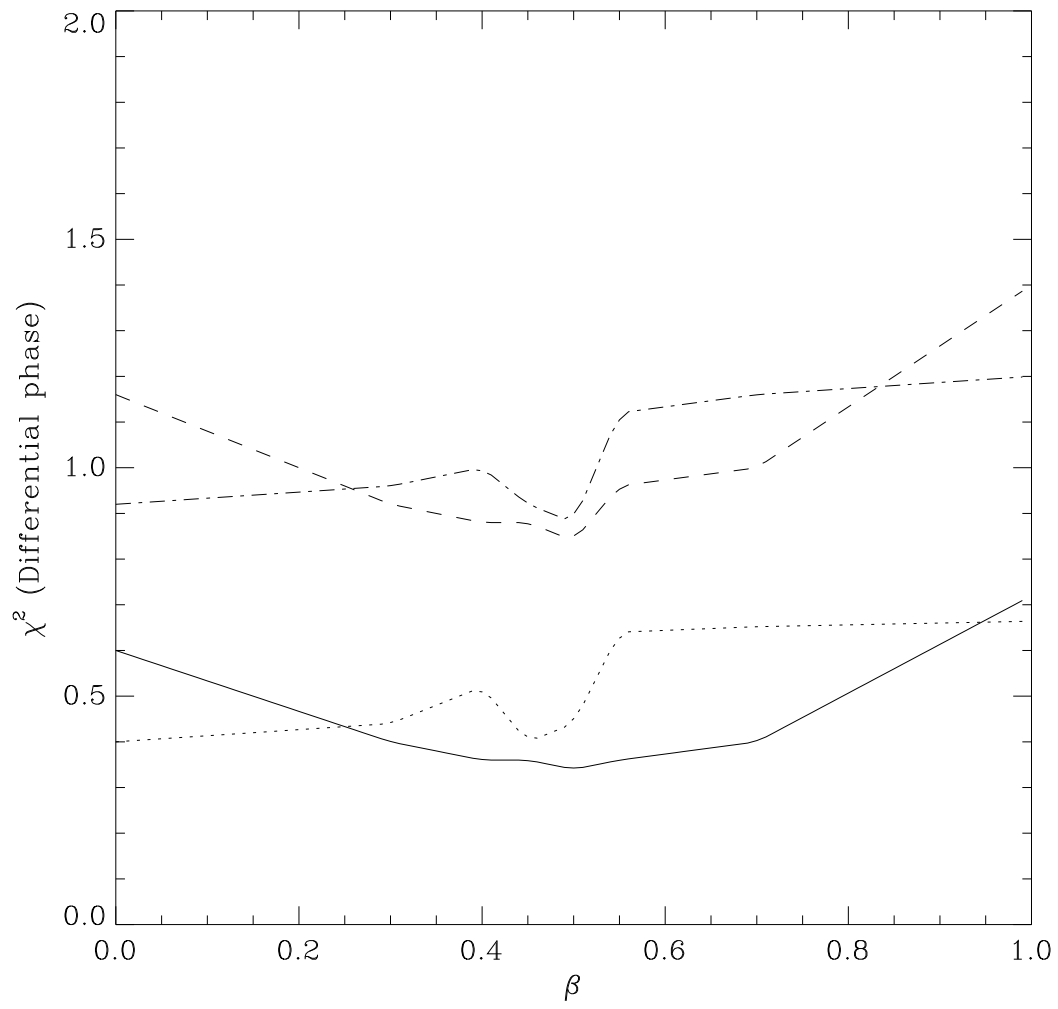
## References

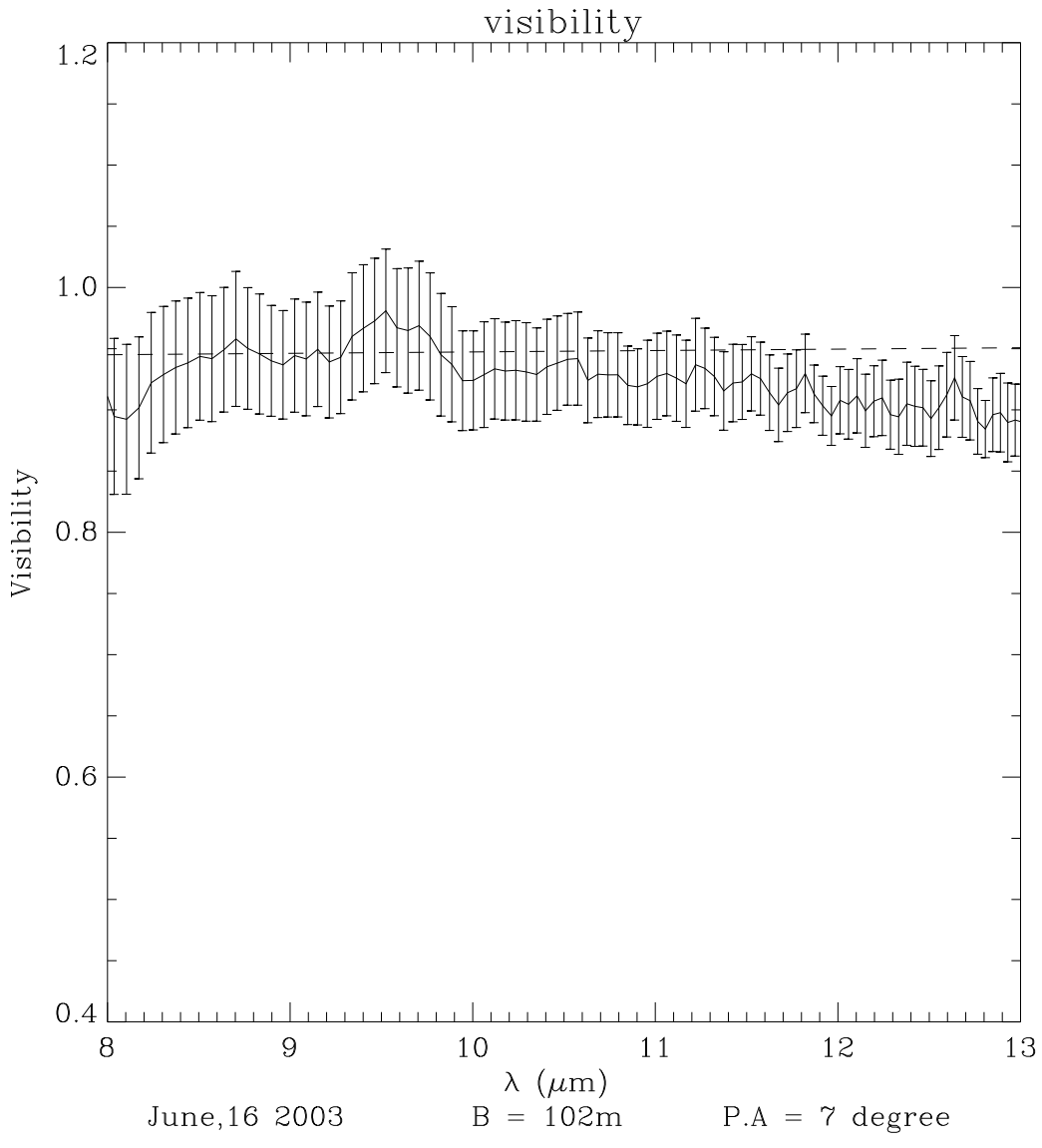
- Araùjo, F.X., Freitas Pacheco, J.A. 1989, MNRAS, 241, 543  
 Bernacca, P.L., & Perinotto, M. 1970, "A catalogue of stellar rotational velocities" Contr. Oss. Astroph. Padova in Asiago, 239, 1  
 Bjorkman, J.E. & Cassinelli, J.P., 1993, ApJ, 409, 429  
 Bjorkman, K.S., Nook, M.A., Nordsieck, K.H., et al., 1997, ApJ, 477, 926  
 Bjorkman, J.E. & Carciofi, A.C. 2004, AAS, 204, 6206 van  
 Boekel, R., Verhoelst, T., Leinert, Ch. et al. 2005, A&A, submitted  
 Castor, J.I, Abbott, D.C., Klein, R.I. 1975, ApJ, 195, 157  
 Chauville, J.; Zorec, J., Ballereau, D. et al., 2001, A&A, 378, 861  
 Chesneau, O., Meilland, A., Rivinius, T. et al., paper I, 2005, A&A, 435, 275  
 Cohen, D.H., Cassinelli, J.P., MacFarlane J.J., 1997, ApJ, 487, 867  
 Cranmer, S.,R. & Owocki, S.P. 1995, ApJ, 440, 308  
 Domiciano de Souza, A., Kervella, P., Jankov, S. et al. 2003, A&A, 407, L47.  
 Dougherty, S.M., Waters, L.B.F.M., Burki, G. et al. 1994, A&A, 290,609  
 Ducati J.R. 2002, "Stellar Photometry in Johnson's 11-color system", Catalogue of Stellar Photometry in Johnson's 11-color system  
 Hanuschik, R.W. 1995, A&A, 423, 434  
 Hanuschik, R.W. 1996, A&A, 308, 170  
 Hanuschik, R.W. 2000, ASPC, 214, 518  
 Hubeny,I. 1988, Computer Physics Comm, 52, 103

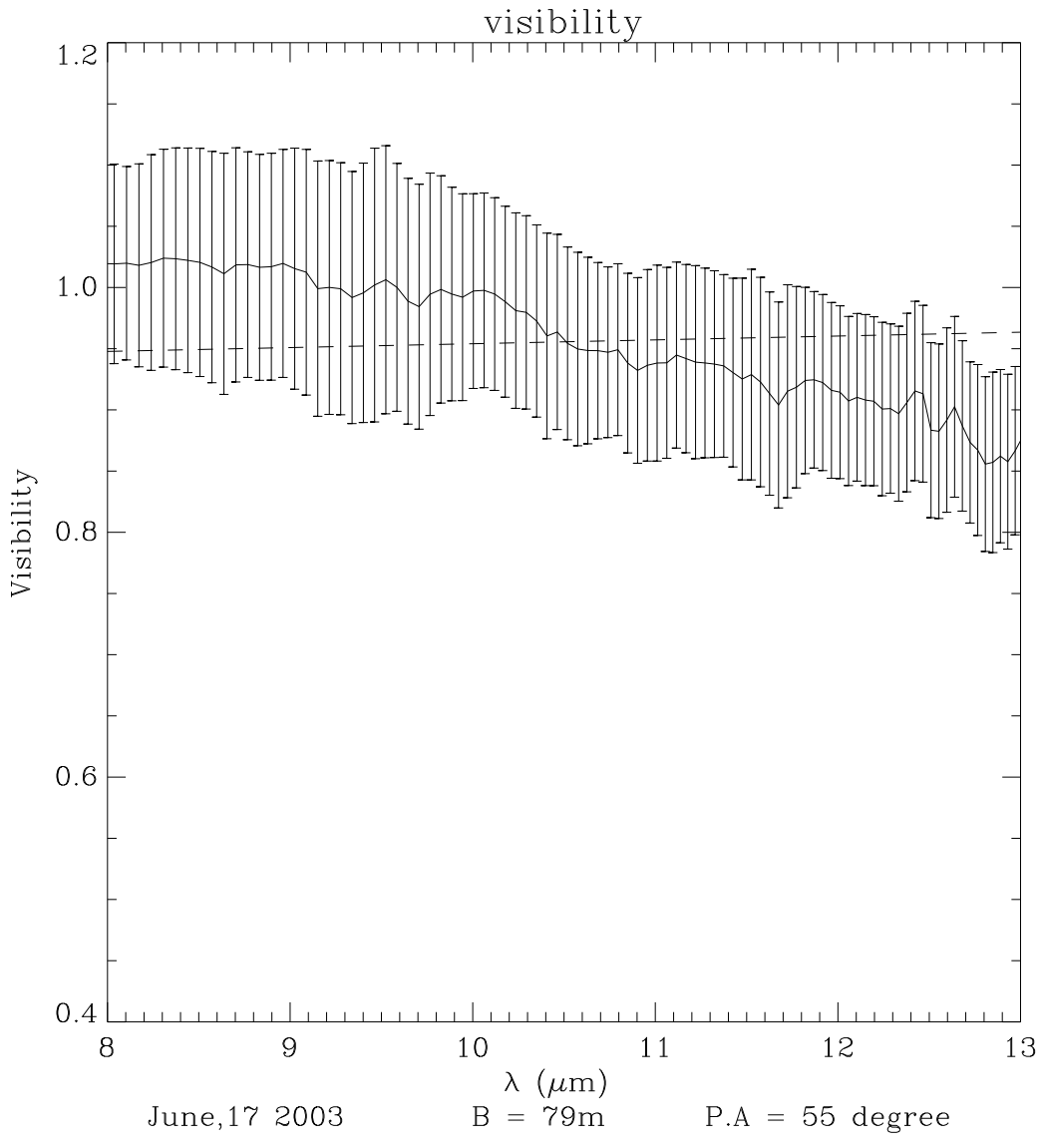
- Hubeny, I. & Lanz, T. 1995, *ApJ*, 439, 875
- Jamar C., Macau-Hercot D., Monfils A., Thompson G.I., Houziaux L., Wilson R., 1976, "UV Bright Star Spectrophotometric Catalog", ESA SR-27
- Johnson H.L., Mitchell R.I., Iriarte B., and Wisniewski W.Z., 1966, "UBV Photometry of Bright Stars" *Commun. Lunar & Planet. Lab.* 4, 99, Table 9.
- Kervella, P. & Domiciano de Souza, A. 2006, *A&A*, in press
- Mc Lean I.S. & Clarke D. 1979, *MNRAS*, 186, 245
- Millour, F., Petrov, R. et al. 2005, *A&A*, in preparation
- Owocki, S.P., Cranmer, S.R. and Blondin, J.M. 1994, *ApJ*, 424, 887
- Owocki, S.P., Cranmer, S.R. and Gayley, K.G. 1996, *ApJ*, 472, L115
- Owocki, S.P. 2005, *ASPC*, 337, 101
- Owocki, S.P. & Gayley, K.G. 1998, *ASPC*, 131, 237
- Perryman, M.A.C., Lindegren, L., Kovalevsky, J. et al. 1997, *A&A* 323, 49
- Poe, C.H. & Friend, D. 1986, *ApJ*, 311, 317
- Poeckert, R. & Marlborough, J.M., *ApJ*, 233, 259
- Porter, J.M. & Rivinius, Th. 2003, *PASP*, 115, 1153
- Quirrenbach, A., Bjorkman, K.S., Bjorkman, J.E. et al., 1997, *ApJ*, 479, 477
- Richichi, A., & Percheron, I. 2002, *A&A*, 386, 492
- Rivinius, Th., Stefl, S., Baade, D. 1999, *A&A*, 348, 831
- Rivinius, Th., Baade, D., Stefl, S. et al. 2001, *A&A*, 379, 257
- Secchi A. 1867, *Astron. Nachrichten*, 68, 63
- Stee, Ph., de Araùjo, F.X. 1994, *A&A*, 292, 221
- Stee, Ph., de Araùjo, F.X., Vakili F. et al. 1995, *A&A*, 300, 219
- Stee, Ph. 1996, *A&A*, 311, 945
- Stee, Ph., Vakili, F., Bonneau, D. et al. 1998, *A&A*, 332, 268
- Stee, Ph. & Bittar, J. 2001, *A&A*, 367, 532
- Stee, Ph., 2003, *A&A*, 403, 1023
- Struve, O. 1931, *ApJ*, 73, 94
- Thomson G.I., Nandy K., Jamar C., Monfils A. Houziaux L., Carnochan D.J., Wilson R., 1978, "Catalogue of stellar ultraviolet fluxes", The Science Research Council, U.K.
- Uesugi, A. & Fukuda, I. 1970, "Catalogue of rotational velocities of the stars" *Contr. Astroph. Kwasan, Obs. Univ. Kyoto*, 189
- Townsend, R.H., Owocki, S.P., Howarth, I.D. 2004, *MNRAS*, 350, 189
- Wood, K., Bjorkman, J.E., Whitney, B.A. & Code, A.D., 1996, *ApJ*, 461, 828
- Wood, K., Bjorkman, J.E., Whitney, B.A. & Code, A.D., 1996, *ApJ*, 461, 847
- Yudin, R.V., Evans, A., 1998, *A&A Sup. Ser.*, 131, 401
- Yudin, R.V. 2001, *A&A*, 368, 912

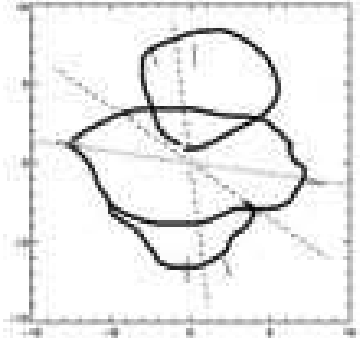
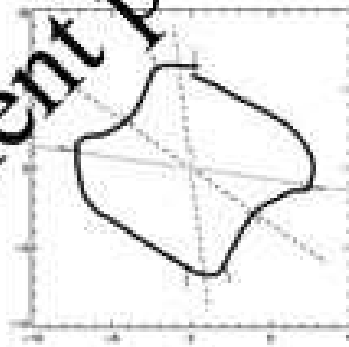
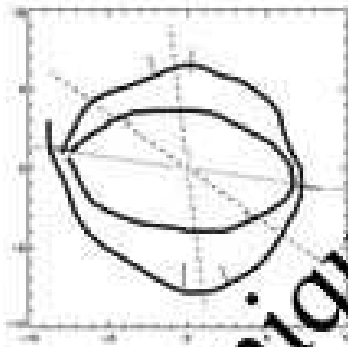
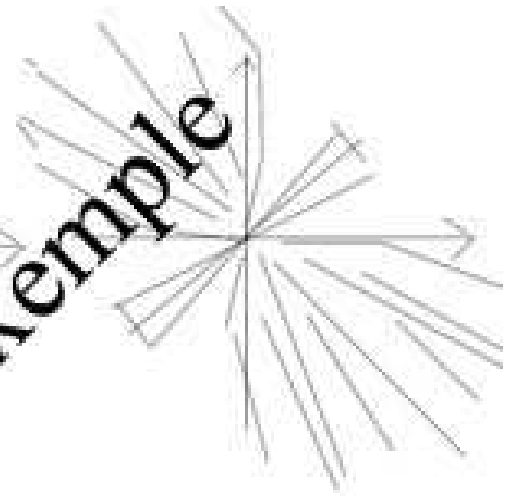
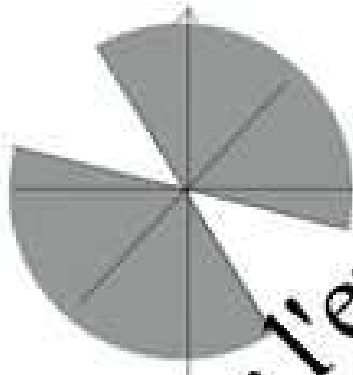
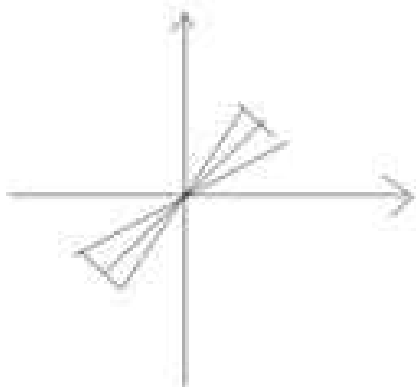












**uniquement pour l'exemple**